CoP Nanoparticles Fabricated Through the Nanoscale Kirkendall Effect Immobilized in 3D Hollow Carbon Frameworks for Oxygen Evolution Reaction

Huang, Wei; Tang, Jing; Diao, Fangyuan; Li, Shuo; Sun, Hongyu; Xiao, Xinxin

Published in:
Journal of the Electrochemical Society

Link to article, DOI:
10.1149/1945-7111/ac2090

Publication date:
2021

Document Version
Peer reviewed version

Cite this paper: https://iopscience.iop.org/article/10.1149/1945-7111/ac2090

CoP nanoparticles fabricated through the nanoscale Kirkendall effect immobilized in 3D hollow carbon frameworks for oxygen evolution reaction

Wei Huang,[1, 2, *] Jing Tang,[3] Fangyuan Diao,[2] Shuo Li,[4] Hongyu Sun,[5] Xinxin Xiao [2, *]

[1] *School of Chemistry and Materials Science, Hunan Agricultural University, Changsha, Hunan, 410128, P. R. China.*

[2] *Department of Chemistry, Technical University of Denmark, DK-2800 Kongens Lyngby, Denmark.*

[3] *College of Environmental Science and Engineering, Hunan University, Changsha 410082, PR China.*

[4] *SDU & Rice Joint Center for Carbon Nanomaterials, Key Laboratory for Liquid-Solid Structural Evolution and Processing of Materials, Ministry of Education, School of Materials Science and Engineering, Shandong University, Jinan 250061, P. R. China.*

[5] *School of Resources and Materials, Northeastern University at Qinhuangdao, Qinhuangdao 066004, PR China.*

* Corresponding authors. E-mail addresses: weihua@hunau.edu.cn (W. Huang), xinxiao@kemi.dtu.dk (X. Xiao).

ABSTRACT: Transition metal phosphides are promising oxygen evolution reaction (OER) catalysts attributed to their earth-abundant and cost-effective features. In this work, nanostructured CoP nanoparticles locked in hollow nitrogen doped carbon frameworks (CoP@HNC) are successfully designed and carefully characterized regarding to morphology, composition and electrochemistry. In a typical low-temperature phosphorization process, the Co species in carbonized poly-dopamine (PDA) coated ZIF-67 are converted to either hollow CoP or small-sized solid CoP nanoparticles governed by the nanoscale Kirkendall effect. The PDA layers derived nitrogen doped carbon components feature a hollow polyhedral structure, with CoP nanoparticles imbedded in the shell. CoP@HNC demonstrates a low overpotential of 327 mV for 10 mA cm^{-2} and a good operational stability (72 h) for alkaline OER. The HNC encapsulation affords the low electronic resistance between CoP nanoparticles, as well as the mechanical and chemical stability of composites by preventing the aggregation of CoP nanoparticles during the OER process.

Keywords: MOF derivates; CoP; Nitrogen doped carbon; Kirkendall effect; OER.

1. Introduction

To tackle the environmental issues and energy crisis associated with the usage of conventional fossil fuels, green energy storage and conversion technologies (batteries, water splitting and fuel cells etc.) are attracting enormous attention.[1-7] Oxygen evolution reaction (OER), constrained by the challenges of large overpotentials and sluggish kinetics, is the crucial reaction in water electrolyzers.[8-10] High-performance OER electrocatalysts with fast kinetics and considerable

stability are thus pivotal. Ir or Ru based materials demonstrate good OER performance but are constrained by the high cost and scarcity in earth crust. It's not surprising that earth-abundant transition metal-based materials for OER catalysts are urgently explored.[11-13]

Transition metal phosphides (TMPs) are emerging as inexpensive OER catalysts.[14-20] However, the pristine TMP, for example CoP, suffers from several inherent shortcomings. For example, the surface atoms of CoP could experience irreversible composition and morphology changes when reacting with hydroxide ions in alkaline media,[21] registering shortened operational lifetime. Bulky CoP demonstrates sluggish reactive kinetics due to a large oxygen adsorption free energy.[22, 23] Accordingly, designing nanostructured CoP is a general strategy to increase the effective working surface area with the associated active sites and thus improved OER catalytic activity.[16, 24] Further, combining CoP with conductive carbon components could promote the electrical conductivity between CoP, and maintain the initial structural stability for long-term OER.[25, 26] For instance, Chen et al. [26] reported that CoP nanosheets grown on the nitrogen-doped graphene (CoP@NG) registered a lower overpotential of 354 mV at 10 mA cm^{-2} for OER, than that of bare CoP (395 mV), and a good stability of 15 h. Therefore, constructing isolated nano-sized CoP locked in the highly conductive carbonaceous matrix with a high active surface area is an effective route for high-performance OER catalysts.

Metal-organic frameworks (MOFs) are a type of nanoporous materials [27-29] and ideal precursors for nanostructured metal-based composites with carbonaceous components.[8, 30-32] Benefiting from the inherited highly abundant porosity and large surface area, the active sites could be exposed as much as possible for catalytic reaction. However, the directly carbonated MOFs derivatives obtained at relatively low annealing temperatures are constrained by the poor

electrical conductivity due to the low crystallization of carbonaceous components. Therefore, rendering highly crystalline carbonaceous components is important.[33-35] For example, Jiang et al. [34] prepared zeolite-type MOF (ZIF-67) derived CoP decorated on reduced graphene oxides, registering an overpotential of 340 mV to obtain 10 mA cm^{-2} and a lifetime of 22 h. Chen et al. [35] annealed a core-shell ZIF-8@ZIF-67 precursor at a relatively high temperature of 920 °C to fabricate CoP nanoparticles encapsulated in a N-doped carbon nanotube hollow polyhedron, exhibiting a low overpotential of 310 mV at 10 mA cm^{-2}, much lower than that of pristine ZIF-67 derived materials (360 mV).

Nanoscale Kirkendall effect for hollow nanomaterial preparation were initially proposed by Yin and co-workers, [36] who successfully synthesized hollow CoX (X = oxygen, sulfur or selenium) nanoparticles from the solution of solid cobalt nanoparticles. The preparation of hollow nanocrystals underwent the Kirkendall effect, i.e. the outer diffusion of cobalt atoms from the core was faster in comparison to the inward diffusion of reactive species. The first report on the solid-phase reaction for hollow nanomaterials involving the nanoscale Kirkendall effect was by Fan et al., [37] who fabricated $ZnAl_2O_4$ spinel nanotubes by annealing core–shell ZnO–Al_2O_3 nanowires in an open quartz tube furnace. These reports spur the utilization of the nanoscale Kirkendall effect as a general strategy for the fabrication of various hollow nanostructures.

Herein, we present nanostructured CoP nanoparticles encapsulated in the nitrogen doped hollow carbon shells prepared via the nanoscale Kirkendall effect for OER. Initially, poly-dopamine (PDA) layers coated polyhedral ZIF-67 (ZIF-67@PDA) composites, in a polyhedral shape with a hollow inner core, are successfully fabricated. In the subsequent carbonization at a relatively high temperature of 900 °C and low-temperature phosphorization process, the Co species are

changed to nanostructured CoP due to the nanoscale Kirkendall effect, generating either hollow CoP or small-sized solid CoP nanoparticles. Besides, PDA derived nitrogen doped carbon layers are obtained, inheriting the hollow polyhedral structure of ZIF-67@PDA. Finally, CoP nanoparticles decorated hollow nitrogen doped carbon frameworks (CoP@HNC composites) are successfully prepared. The CoP@HNC composites register an overpotential of 327 mV for 10 mA cm^{-2} and a durability of 72 h for OER.

2. Experimental section

Fabrication of CoP@HNC composites. ZIF-67@PDA composites were synthesized following our previous report [38] (Scheme 1). ZIF-67 samples were prepared by mixing $Co(NO_3)_2 \cdot 6H_2O$ (1.71 mM, 99%, Aladdin) and 2-methylimidazole (8.0 mM, 98%, Aladdin) in methanol (100 mL, ≥ 99.5%, Sinopharm) and aged at room temperature (RT) for one day. The washed ZIF-67 samples (120 mg) were added in 10 mM pH 8.5 Tris-HCl (50 mL, Aladdin) solution containing dopamine hydrochloride (DAH, 50 mg, 98%, Aladdin), which was sonicated for 10 min and subsequently stirred for one day at RT. ZIF-67@PDA composites were washed and collected, which were carbonized at 900 °C for 3 h under Argon atmosphere. Phosphorization was performed at 350 °C for 2 h under Argon with a NaH_2PO_2 (99%, Aladdin) boat seating in the upstream of the boat containing the annealed products, resulting in CoP@HNC. Control samples like the CoP/C composites were also fabricated by the same protocol but without the PDA coating.

Morphology and composition characterization. Scanning (SEM, Quanta FEG 200 ESEM, 15 kV) and transmission electron microscopy (TEM, Tecnai G2 T20, 200 kV) were performed to study the microstructures. Crystalline structures of the synthetic samples were measured by X-ray diffraction (XRD, Miniflex 600, Cu-Kα radiation, λ = 1.5418 Å). A Thermo-Scientific X-ray

photoelectron spectroscope (XPS, Al-Kα radiation, 1484.6 eV) was used to analyze the surface composition and chemical bonding state. Raman spectroscopy (Renishaw InVia Raman spectrometer, 633 nm Laser) analysis was tested for carbon status in the sample. A surface area & pore size analyzer (ASAP 2020, Micromeritics) was used to measure the specific surface area.

Electrochemical measurements. Glassy carbon-based rotating disk electrodes (RDE, d = 5.0 mm) were polished with Al_2O_3 slurries and used as the working electrode. Active materials (2 mg) and Nafion solution (25 µL, 10 wt%) were mixed in ultrapure water (975 µL) by 1 h sonication to prepare the uniform catalyst ink. 15 µL of the ink was then drop-cast onto the RDE and dried under RT. Electrochemical characterization was performed in a three-electrode system on an Autolab PGSTAT12. The electrolyte was 1.0 M KOH. A graphite rod (d: 3 mm) and a Ag/AgCl served as the counter and reference electrode, respectively. A Pine Instrument rotating system was used to control the rotation speed of RDE. Compensation of the polarization potentials were carried out based on the relationship between the solution resistance (R_s) and registered current (I) via: $E_{Ag/AgCl\text{-}corr} = E_{Ag/AgCl} - IR_s$.[39] To obtain R_s, electrochemical impedance spectroscopy (EIS) (frequency range: 0.1 Hz - 100 kHz; applied potential: 1.553 V vs. reversible hydrogen electrode (RHE)) was performed. All reported potentials were against RHE and calibrated with the relationship: $E_{RHE} = E_{Ag/AgCl\text{-}corr} + 0.197 + 0.059 \times pH$. Oxygen gas (purity ≥ 99.995%) was maintained in the electrolyte to maintain the O_2/H_2O equilibrium at 1.23 V vs. RHE. The OER overpotential was determined by the relationship: $\eta = E_{RHE} - 1.23$ V. In order to decrease interference from generated gas bubbles, linear sweep voltammetry (LSV) was performed at a relatively slow scan rate of 1 mV s^{-1} and a stable rotation speed of 1600 rpm. The catalyst ink of CoP@HNC was coated on the Ni foam (thickness: 300 µm, catalyst loading: 0.5 mg cm^{-2}) for the durability measurement,

which was tested by chronopotentiometry at 10 mA cm^{-2}. Tafel slope (b) was determined according to the Tafel equation: [40, 41]

$$\eta = a + b \cdot \log j \quad (2.1)$$

CVs at different scan rates of 20, 40, 60, 80, 100 and 120 mV s^{-1} in a potential window of 0.15-0.35 V vs. RHE, where no OER occurring, were recorded to calculate the electrochemical double-layer capacitance (C_{dl}). The values of $\Delta j = (j_a - j_c)$, where j_a and j_c are the anodic and cathodic current density respectively, are summarized at 0.25 V vs. RHE. Δj shows a linear relationship against the corresponding scan rate, whose slope is twice of the value of C_{dl}.

3. Results and discussion

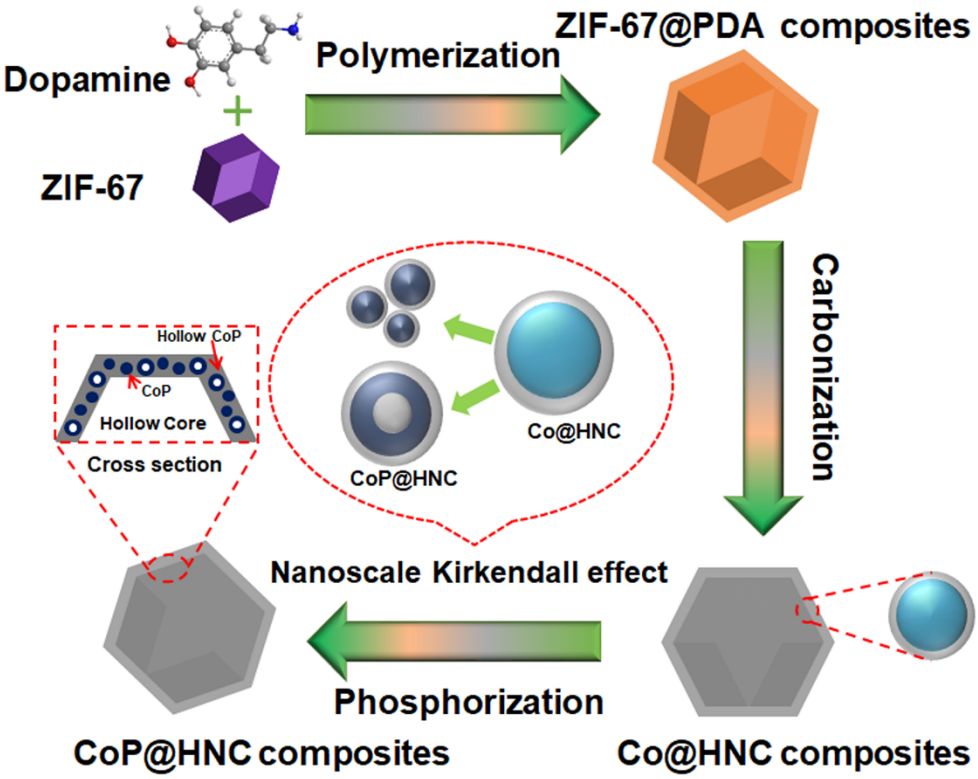

Scheme 1. Schematic drawing of the synthesis of CoP@HNC. Not drawn to real scale.

Formation process and crystalline structure. The overall synthetic process of CoP@HNC composites is depicted in Scheme 1. The hollow ZIF-67@PDA composites are first prepared according to our previous report.[38] The polymerization of PDA is accompanied with the dissolution of the inside ZIF-67 crystals. Co@HNC composites are then obtained by carbonizing ZIF-67@PDA at 900 °C under Argon, inheriting the previous hollow structure with embedded Co nanoparticles. In the subsequent phosphorization process, Co nanoparticles are converted into either hollow or smaller-sized solid CoP nanoparticles due to the nanoscale Kirkendall effect,[42] leading to the final CoP nanoparticles immobilized in hollow nitrogen doped carbon frameworks (CoP@HNC composites).

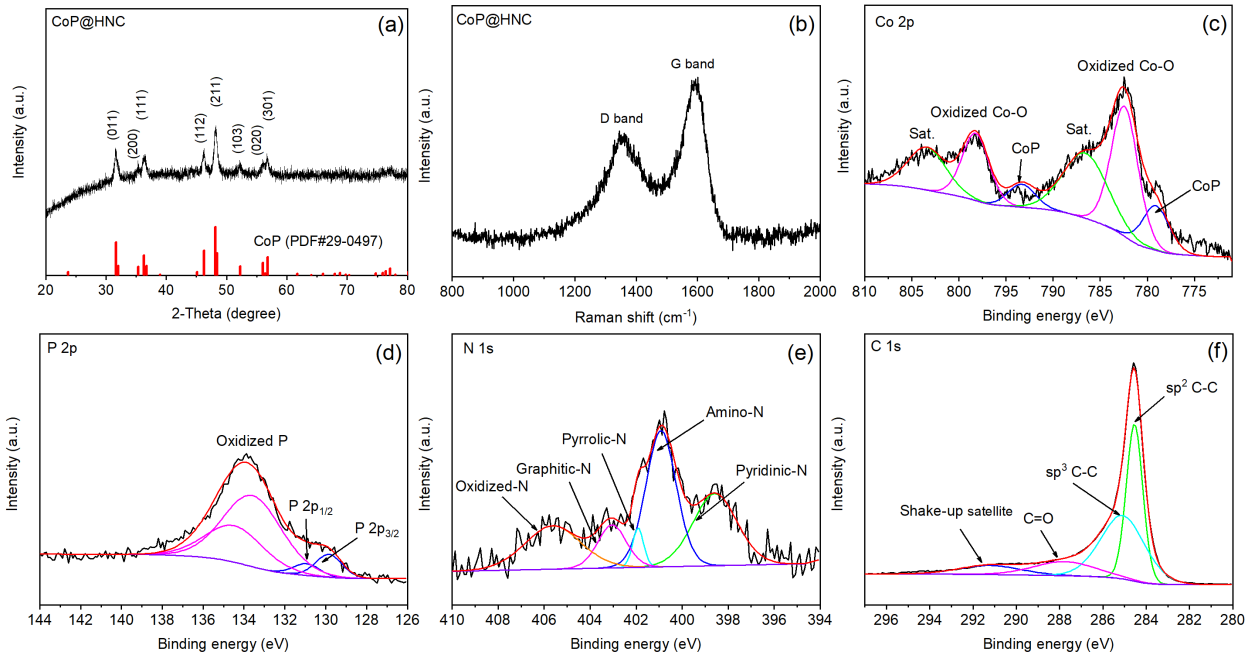

Figure 1. XRD pattern (a) and Raman spectrum (b) of CoP@HNC. High-resolution Co 2p (c), P 2p (d), N 1s (e) and C1s (f) XPS spectra of CoP@HNC.

The crystalline structure of CoP@HNC is initially investigated by XRD. The diffraction peaks of CoP@HNC composites (Figure 1a) at 31.6°, 35.3°, 36.3°, 46.2°, 48.1°, 52.3°, 56.0° and 56.8° match well with the (011), (200), (111), (112), (211), (103), (020) and (301) crystalline planes of CoP (JCPDS No. 29-0497),[35, 43] respectively. Besides, the Raman spectrum of CoP@HNC (Figure 1b) shows the obvious carbon signals, which is similar to that of graphene. The D band (1356 cm^{-1}) reflects the disordered graphite, while the G band (1594 cm^{-1}) is originated from the vibration of the sp^2 hybridized carbon bonding.[38, 44] Higher intensity of G band than D band indicates the high graphitization degree of CoP@HNC composites for good electrical conductivity. The surface chemical bonding states of CoP@HNC composites are studied carefully by XPS. The survey spectrum (Figure S1) exhibits clear elemental signals of Co, C, P, N and O. The high-resolution Co 2p spectrum finds peaks at 779.1 and 793.3 eV, which are due to the chemical bonding of CoP (Figure 1c). Another doublet of peaks at 782.4 and 798.2 eV is from the oxidized Co-O species, which can be rationalized by the partial oxidization of Co species on the surface. Peaks at 786.6 and 803.4 eV belong to the accompanied satellite peaks.[25, 35] The high-resolution P 2p spectrum (Figure 1d) is deconvoluted into two doublets at 129.8/130.9 eV and 133.6/134.5 eV, matching the P $2p_{3/2}$ (P $2p_{1/2}$) and the presence of oxidized P on the surface, respectively.[24, 25, 45] Four peaks at 398.1, 398.6, 401.0 and 405.2 eV are identified in high-resolution N 1s spectrum (Figure 1e), assigning to the signals of pyridinic, pyrrolic, graphitic and oxidized-N, respectively. N doping in the composites is beneficial to improve the electrical conductivity between CoP nanoparticles bridged by the strong interaction mediated with N.[21, 38] In the high-resolution C 1s spectrum (Figure 1f), peaks at 284.5 and 285.1 eV are related to the sp^2 and sp^3 C-C bonding, respectively.

The other characteristic peaks at 287.8 and 291.2 eV are ascribed to the vibration of C=O bonding and the signal of shake-up satellite peak, respectively.[21, 46]

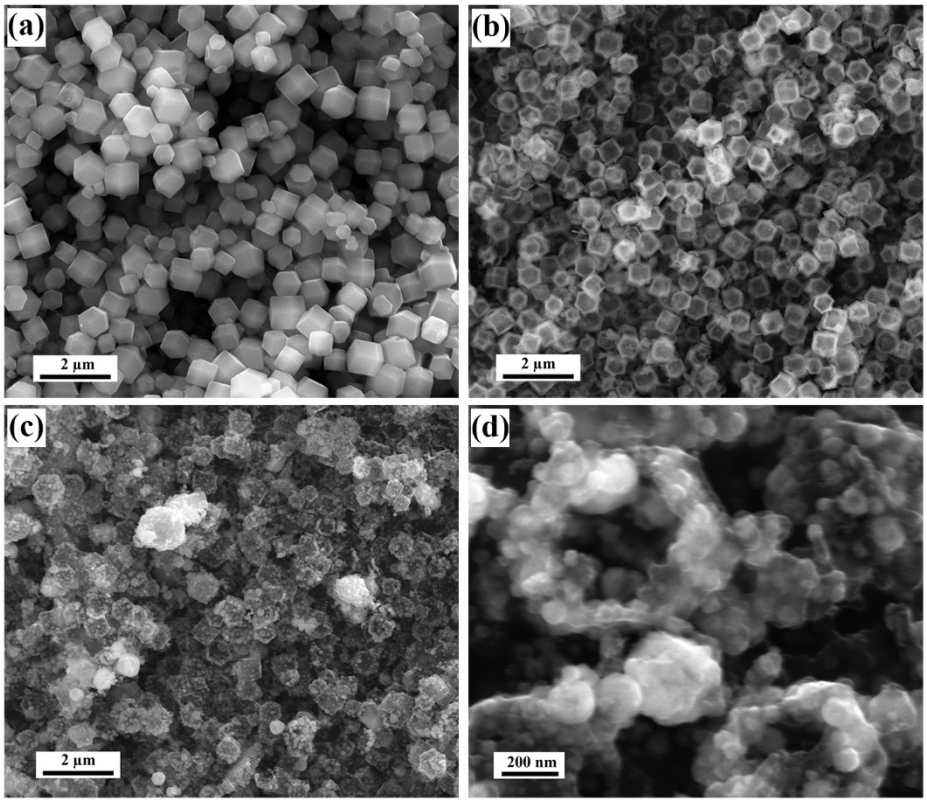

Figure 2. SEM characterization of (a) ZIF-67, (b) ZIF-67@PDA and (c-d) CoP@HNC.

Morphology and surface area analysis. Morphology characterization of the synthetic materials is carried out by electron microscopy. SEM and TEM images of ZIF-67 crystals (Figure 2a, 3a and 3d) demonstrate a polyhedral shape. After polymerization, the original polyhedral structure is maintained in the ZIF-67@PDA composites (Figure 2b, 3b and 3e), with the hollow structure validated by the corresponding TEM images (Figure 3b and 3e). The SEM image of Co@HNC is shown in Figure S2, suggesting the surface of polyhedral structure becomes rougher than that of ZIF-67@PDA, with obvious small particles observed on the surface. The carbonization allows the

transformation of the organic ligands in ZIF-67@PDA into carbon layers for enhanced electrical conductivity, beneficial for the OER process. Furthermore, SEM images of CoP@HNC (Figure 2c and 2d) indicate the rough surface of polyhedral structure is efficiently maintained. During the annealing process, the structure would partially shrink due to the transformation of organic ligands to the nitrogen-doped carbon layers. Thus, the average size of CoP@HNC (700±100 nm) is smaller than those of ZIF-67 (1000±200 nm) and ZIF-67@PDA (1000±100 nm). Figure 3c and 3f demonstrate that hollow carbon shells are decorated with either hollow or solid small-sized CoP nanoparticles. As a control, TEM images of Co@HNC (Figure S3) exhibit that only solid Co nanoparticles are encapsulated by the hollow carbon shells. This observation reveals the transformation of Co to CoP nanoparticles follows the nanoscale Kirkendall effect during phosphorization. CoP thin layer is initially generated over the metallic Co nanocrystals. Co cations with a small ionic radius diffuse outward faster over PH_3 gas molecules diffuse inward. The Kirkendall voids are formed near the Co/CoP interface during the vacancy-assisted exchange of the composites via bulk interdiffusion.[36, 42] The Co nanocrystals convert to hollow CoP nanostructures via Kirkendall-type diffusion. In addition, a fraction of relatively large nanoparticles would be broken into small-sized solid CoP nanoparticles. The associated selected area electron diffraction (SAED) (inset of Figure 3f) exhibits the typical (200), (211) and (020) crystalline planes of CoP (JCPDS No. 29-0497).[24, 25] The high-resolution TEM image (Figure 3g) indicates that CoP nanoparticles are enclosed by carbon layers, and the interplanar spacing is measured to be 0.253 nm, assigning to the (200) lattice fringe of CoP.[24] The low-resolution STEM image (Figure 3h) suggests that isolated CoP nanoparticles are interconnected by carbon shells. Besides, hollow CoP nanoparticles are obviously visible in the high-resolution STEM image (Figure

3i). The companying energy-dispersive X-ray spectroscopy (EDS) mapping (Figure 3j-n) sees the uniform location of elemental Co, P, C, N and O, in consistent to the XPS analysis. Besides, the elemental Co (Figure 3j) and P (Figure 3k) signals are more intense in the outside than the inner region, further suggesting the formation of hollow CoP nanoparticles.

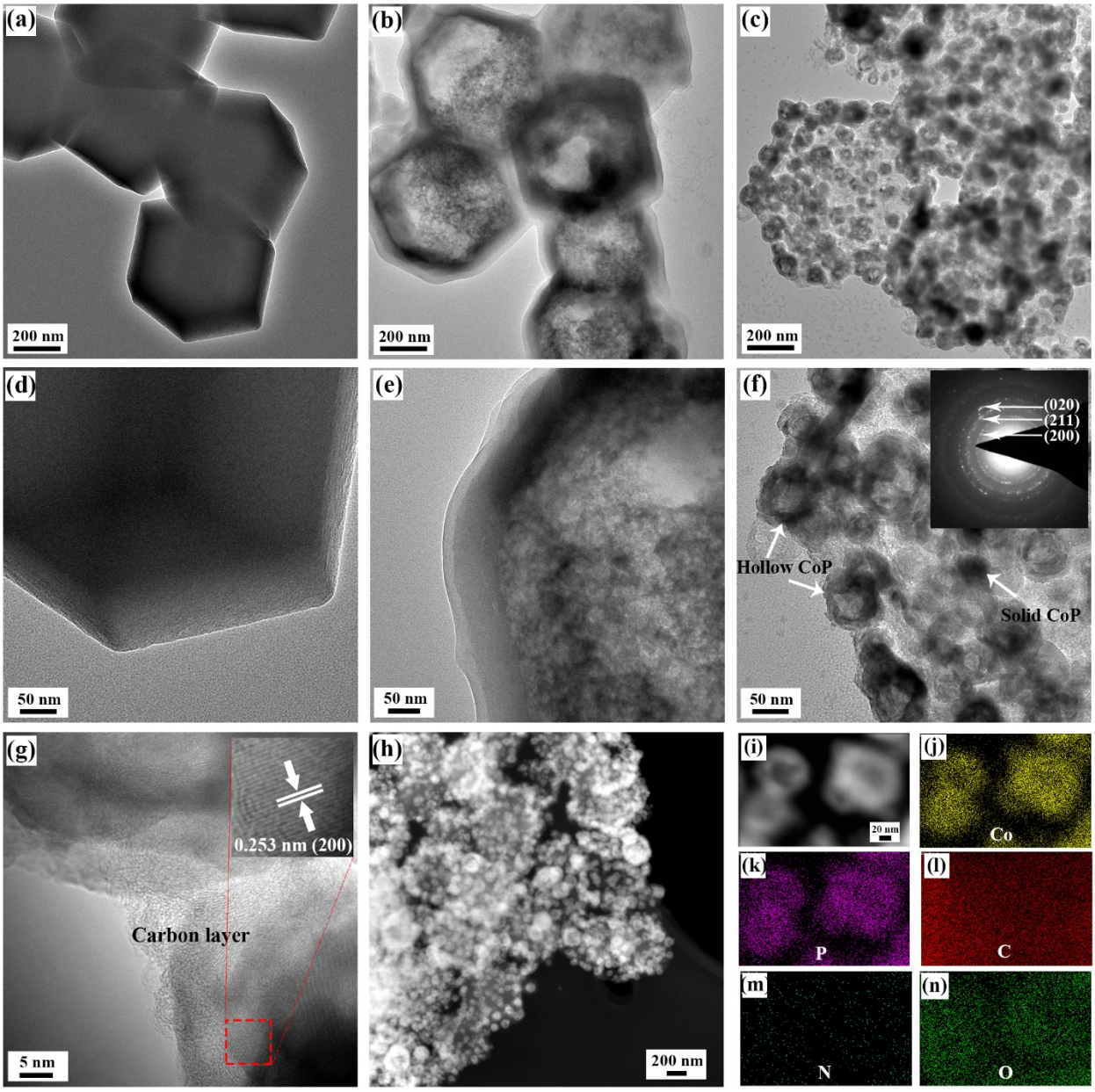

Figure 3. Low-resolution TEM images of (a, d) ZIF-67, (b, e) ZIF-67@PDA and (c, f) CoP@HNC. The SAED image of CoP@HNC composites is inserted in Figure 3f. (g) High-resolution TEM image, (h) STEM image and (i-n) corresponding EDS mapping images of CoP@HNC.

The specific surface area, as well as the pore-size distribution, of CoP@HNC composites is analyzed by BET measurement. The typical nitrogen adsorption–desorption isotherm of CoP@HNC (Figure S4a) implies a hybrid type (I, II and IV), with a calculated specific surface area of 136.9 $m^2 g^{-1}$. The rapid rise in the relatively low pressure confirms the presence of microspore (< 2 nm) due to the presence of carbon shells. The hysteresis loop in the isotherm is attributed to the mesoporous (2–50 nm) structure in the composites. The sharp rise in the relatively high pressure is assigned to the macropores (> 50 nm) from the hollow carbon frameworks. The pore-size distribution profile (Figure S4b) further verifies the existence of microspores, mesopores and macropores in CoP@HNC. The hybrid porous structure could improve the contact area between active sites and electrolyte for good catalytic activity.

Electrochemical performance for OER.

The OER electrochemical performance of synthetic samples is investigated by LSV test in a typical three-electrode system containing O_2-saturated 1 M KOH at 1 mV s^{-1}. As displayed in Figure 4a, CoP@HNC exhibits a low overpotential of 327 mV at a typical current density of 10 mA cm^{-2}. ZIF-67 requires an overpotentials of 443 mV at 5 mA cm^{-2}. ZIF-67@PDA and Co@HNC demonstrate overpotentials of 393 and 380 mV at 10 mA cm^{-2}, respectively. CoP@HNC shows lower overpotential than that of the pristine CoP/C with a cracked structure (Figure S4) registering 379 mV and the commercial RuO_2 (340 mV). This confirms that the role of hollow porous structure

provides abundant OER active sites. In addition, CoP@HNC (Figure 4b) shows a Tafel slope of 50 mV dec^{-1}, also lower than those of the ZIF-67 (177 mV dec^{-1}), ZIF-67@PDA (106 mV dec^{-1}), Co@HNC (78 mV dec^{-1}), pristine CoP/C (77 mV dec^{-1}) and commercial RuO_2 (74 mV dec^{-1}), another proof of a fast OER on CoP@HNC.[40] Chronopotentiometry is further used to study the operational stability of CoP@HNC at 10 mA cm^{-2}, with negligible changes in operational potential in a time course of 72 h. In contrast to previous reports (Table S1) on CoP based materials used for OER, CoP@HNC exhibits a comparable overpotential to generate 10 mA cm^{-2} and good catalytic stability. The enhanced stability of CoP@HNC is mainly attributed to the monodispersed hollow CoP and small-sized solid CoP nanoparticles are distributed uniformly in the carbon layers, which can efficiently buffer the agglomeration of active materials and facilitate the charge transfer for a good OER stability. The carbon layers can hinder aggregation and pulverization of CoP nanoparticles.

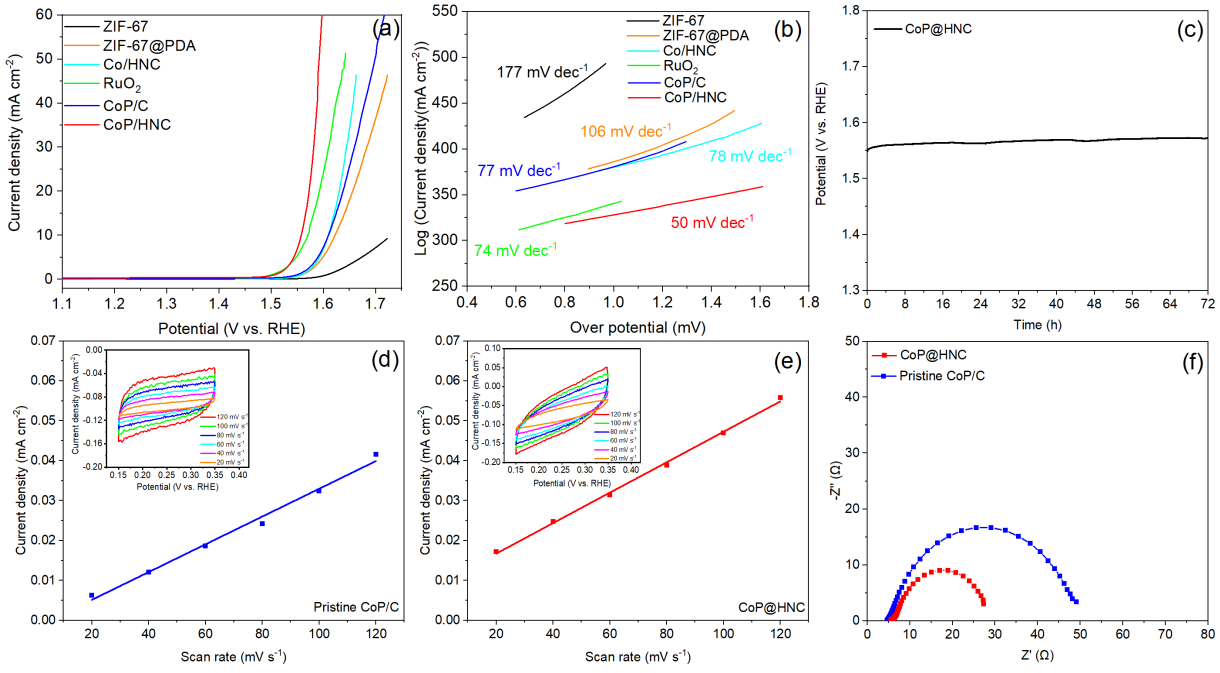

Figure 4. (a) LSVs of ZIF-67, ZIF-67@PDA, Co@HNC, RuO_2, pristine CoP/C and CoP@HNC in O_2-saturated 1.0 M KOH at 1 mV s^{-1}. (b) The corresponding Tafel plots derived from (a). (c) Chronopotentiometric response of CoP@HNC composites at 10 mA cm^{-2}. Current density vs. scan rate for (d) pristine CoP/C and (e) CoP@HNC. Insets are the CV curves for pristine (d) CoP/C and (e) CoP@HNC in a small potential range in O_2-saturated 1 M KOH at a series of scan rates from 20 to 120 mV s^{-1}, respectively. (f) Nyquist plots of CoP@HNC and pristine CoP/C measured at 1.553 V vs. RHE.

The electrochemically active surface area (ECSA) is estimated according to the measurement of C_{dl}, which is likely to be related to the surface density of active sites.[47] The C_{dl} of pristine CoP/C (Figure 4d) is determined to be 174 µF cm^{-2}, lower than 190 µF cm^{-2} of CoP@HNC (Figure 4e). EIS (Figure 4f) is further carried out to study the interfacial charge transfer kinetics, with the diameter of the semicircles of the Nyquist plot determined as the charge transfer resistance (R_{ct}).[44] R_{ct} of CoP@HNC (25 Ω) is much smaller than that of pristine CoP/C (47 Ω), suggesting a much faster charge transfer for CoP@HNC as the OER catalyst. In comparison to the CoP/C, the hollow structure of CoP@HNC exhibits abundant active sites for the OER as validated by the ECSA results, leading to faster charge transfer. Besides, the nitrogen-doped carbon derived from the PDA is expected to improve the internal electrical conductivity. [21, 38] Thus CoP@HNC offers a faster charge transfer over CoP/C.

The OER reaction mechanism of CoP@HNC are shown in Figure 5. [35, 48] OH^- in the alkaline solution steadily contacts with the surface of CoP in the CoP@HNC during the OER process. One active site (*) on the CoP surface reacts with OH^-, forming different OER intermediates (*OH, *O and

*OOH) absorbed on active sites, finally generating O_2. The whole reaction process is summarized in the following equations.

$$4OH^- \rightarrow 2H_2O + O_2 + 4e^- \quad (3.1)$$

$$OH^- + X^* \rightarrow X^*OH + e^- \quad (3.2)$$

$$X^*OH + OH^- \rightarrow X^*O + H_2O + e^- \quad (3.3)$$

$$X^*O + OH^- \rightarrow X^*OOH + e^- \quad (3.4)$$

$$X^*OOH + OH^- \rightarrow X^* + O_2 + H_2O + e^- \quad (3.5)$$

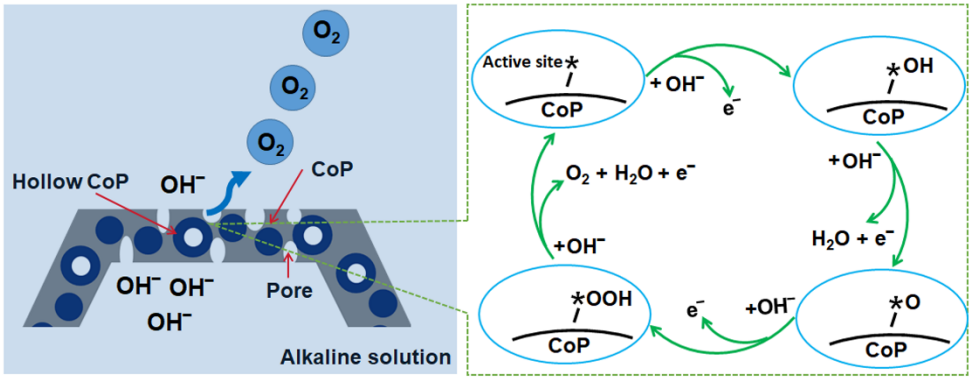

Figure 5. Schematic drawing of the OER reaction mechanism on the surface of CoP. Not drawn to real scale.

To study the morphology and composition change of CoP@HNC after long-term OER, the active materials after durability test have been further studied by SEM and XPS. The SEM image (Figure S6a) indicates the surfaces of composites become smoother with the disappearance of CoP particles (Figure 2c). Besides, the corresponded EDS mappings (Figure S6b-e) show the much lower signal intensity of P signal than that of Co, further suggesting the decomposition of CoP during the OER process. In addition, the high-resolution Co 2p spectrum (Figure S6f) after durability test is mainly contributed by the oxidized Co-O species, revealing the transformation of CoP to cobalt based oxy-hydroxides. Further, the disappeared P signal in high-resolution P 2p

spectrum (Figure S6g) after durability test is consistent to the EDS mapping (Figure S6c). These observations imply that the main active sites in the CoP@HNC composites are from Co species. The surface CoP would transform to a thin layer of metal hydroxides/oxy-hydroxides for catalytic reaction during alkaline OER process. The inner residual CoP core assists with fast electron transfer.[21, 35, 49]

4. Conclusions

Nanostructured CoP nanoparticles locked in the nitrogen doped hollow carbon frameworks (CoP@HNC composites) are successfully designed. The nanoscale Kirkendall effect has been identified to govern the preparation of nanostructured CoP nanoparticles from the Co species in the precursor. CoP@HNC shows an efficient OER performance with a low overpotential of 327 mV at 10 mA cm^{-2} and a long-term durability of 72h. The good catalytic activity could be explained by the abundant active sites brought by the exposed encapsulated CoP nanoparticles and highly conductive hollow nitrogen doped carbon frameworks of CoP@HNC. Our approach represents a new route to construct novel nanostructured transition metal phosphides/carbon composites for OER.

Declaration of competing interest

The authors declare no competing financial interest.

Acknowledgment

The work is supported by Chinese Scholarship Council (201706220080) and The Danish Council for Independent Research for the YDUN project (DFF 4093-00297). X.X. acknowledges the Villum Experiment (grant No. 35844).

References

1. Z. H. Lei, J. M. Lee, G. Singh, C. I. Sathish, X. Z. Chu, A. H. Al-Muhtaseb, A. Vinu and J. B. Yi, *Energy Storage Mater.*, **36**, 514 (2021).
2. K. Wang, K. N. Hui, K. S. Hui, S. Peng and Y. Xu, *Chem. Sci.* (2021).
3. Y. H. Tian, Z. C. Yu, L. Y. Cao, X. L. Zhang, C. H. Sun and D. W. Wang, *J. Energy Chem.* , **55**, 323 (2021).
4. W. Huang, X. Zheng, H. Shangguan, X. Xiao, J. Tang, H. Sun, K. Mølhave, L. Ci, P. Si and J. Zhang, *Appl. Surf. Sci.*, **525**, 146513 (2020).
5. J. Tang, R. M. L. Werchmeister, L. Preda, W. Huang, Z. Zheng, S. Leimkühler, U. Wollenberger, X. Xiao, C. Engelbrekt, J. Ulstrup and J. Zhang, *ACS Catal.*, **9**, 6543 (2019).
6. Y. Yang, S. Li, W. Huang, H. Shangguan, C. Engelbrekt, S. Duan, L. Ci and P. Si, *J. Mater. Chem. A*, **7**, 14670 (2019).
7. J. Theerthagiri, A. P. Murthy, S. J. Lee, K. Karuppasamy, S. R. Arumugam, Y. Yu, M. M. Hanafiah, H.-S. Kim, V. Mittal and M. Y. Choi, *Ceram. Int.*, **47**, 4404 (2021).
8. W. Huang, J. Tang, F. Diao, C. Engelbrekt, J. Ulstrup, X. Xiao and K. Mølhave, *ChemElectroChem*, **7**, 4695 (2020).
9. X.-M. Liu, X. Cui, K. Dastafkan, H.-F. Wang, C. Tang, C. Zhao, A. Chen, C. He, M. Han and Q. Zhang, *J. Energy Chem.* , **53**, 290 (2021).
10. W. Huang, C. Peng, J. Tang, F. Diao, M. Nulati Yesibolati, H. Sun, C. Engelbrekt, J. Zhang, X. Xiao and K. S. Mølhave, *J. Energy Chem.*, **65**, 78 (2022).
11. W. M. Li, C. Wang and X. F. Lu, *J. Mater. Chem. A*, **9**, 3786 (2021).
12. Q. N. Liang, J. M. Chen, F. L. Wang and Y. W. Li, *Coord. Chem. Rev.*, **424**, 24 (2020).
13. H. M. Sun, Z. H. Yan, F. M. Liu, W. C. Xu, F. Y. Cheng and J. Chen, *Adv. Mater.*, **32**, 18 (2020).
14. B. Kim, T. Kim, K. Lee and J. H. Li, *ChemElectroChem*, **7**, 3578 (2020).
15. Y. Li, R. P. Li, D. Wang, H. Xu, F. Meng, D. R. Dong, J. Jiang, J. Q. Zhang, M. Z. An and P. X. Yang, *Int. J. Hydrog. Energy*, **46**, 5131 (2021).
16. G. Zhou, M. Li, Y. Li, H. Dong, D. Sun, X. Liu, L. Xu, Z. Tian and Y. Tang, *Adv. Funct. Mater*, **30**, 1905252 (2020).
17. Z. Cui, J. Lin, J. Wu, J. Yu, J. Si and Q. Wang, *J. Alloys Compd.*, **854**, 156830 (2021).
18. B. You, N. Jiang, M. Sheng, S. Gul, J. Yano and Y. Sun, *Chem. Mater.*, **27**, 7636 (2015).
19. P. Rekha, S. Yadav and L. Singh, *Ceram. Int.* (2021).
20. S. D. Ghadge, O. I. Velikokhatnyi, M. K. Datta, K. Damodaran, P. M. Shanthi and P. N. Kumta, *J. Electrochem. Soc.*, **168**, 064512 (2021).
21. X. Wang, Z. Ma, L. Chai, L. Xu, Z. Zhu, Y. Hu, J. Qian and S. Huang, *Carbon*, **141**, 643 (2019).
22. L. Zhou, M. Shao, J. Li, S. Jiang, M. Wei and X. Duan, *Nano Energy*, **41**, 583 (2017).
23. K. Zhang, G. Zhang, Q. Ji, J. Qu and H. Liu, *Nano-Micro Lett.*, **12**, 154 (2020).
24. Z. Liang, W. Zhou, S. Gao, R. Zhao, H. Zhang, Y. Tang, J. Cheng, T. Qiu, B. Zhu, C. Qu, W. Guo, Q. Wang and R. Zou, *Small*, **16**, 1905075 (2020).
25. Y. Bai, H. Zhang, Y. Feng, L. Fang and Y. Wang, *J. Mater. Chem. A*, **4**, 9072 (2016).
26. Y. Lu, W. Hou, D. Yang and Y. Chen, *Electrochim. Acta*, **307**, 543 (2019).
27. A. Bavykina, N. Kolobov, I. S. Khan, J. A. Bau, A. Ramirez and J. Gascon, *Chem. Rev.*, **120**, 8468 (2020).

28. *Chem. Rev.*, **112**, 673 (2012).
29. W. Huang, S. Li, X. Cao, C. Hou, Z. Zhang, J. Feng, L. Ci, P. Si and Q. Chi, *ACS Sustainable Chem. Eng.*, **5**, 5039 (2017).
30. H. F. Wang, L. Y. Chen, H. Pang, S. Kaskel and Q. Xu, *Chem. Soc. Rev.*, **49**, 1414 (2020).
31. H. Z. Luo, Z. T. Zeng, G. M. Zeng, C. Zhang, R. Xiao, D. L. Huang, C. Lai, M. Cheng, W. J. Wang, W. P. Xiong, Y. Yang, L. Qin, C. Y. Zhou, H. Wang, Y. Zhou and S. H. Tian, *Chem. Eng. J.*, **383**, 20 (2020).
32. W. P. Yang, X. X. Li, Y. Li, R. M. Zhu and H. Pang, *Adv. Mater.*, **31**, 35 (2019).
33. L. Du, L. X. Xing, G. X. Zhang and S. H. Sun, *Carbon*, **156**, 77 (2020).
34. L. Jiao, Y.-X. Zhou and H.-L. Jiang, *Chem. Sci.*, **7**, 1690 (2016).
35. Y. Pan, K. Sun, S. Liu, X. Cao, K. Wu, W.-C. Cheong, Z. Chen, Y. Wang, Y. Li, Y. Liu, D. Wang, Q. Peng, C. Chen and Y. Li, *J. Am. Chem. Soc.*, **140**, 2610 (2018).
36. Y. Yin, R. M. Rioux, C. K. Erdonmez, S. Hughes, G. A. Somorjai and A. P. Alivisatos, *Science*, **304**, 711 (2004).
37. H. Jin fan, M. Knez, R. Scholz, K. Nielsch, E. Pippel, D. Hesse, M. Zacharias and U. Gösele, *Nat. Mater.*, **5**, 627 (2006).
38. H. Shangguan, W. Huang, C. Engelbrekt, X. Zheng, F. Shen, X. Xiao, L. Ci, P. Si and J. Zhang, *Energy Storage Mater.*, **18**, 114 (2019).
39. Z.-F. Huang, J. Song, Y. Du, S. Xi, S. Dou, J. M. V. Nsanzimana, C. Wang, Z. J. Xu and X. Wang, *Nat. Energy*, **4**, 329 (2019).
40. A. J. Bard and L. R. Faulkner, *Electrochemical Methods: Fundamentals and Applications (2nd ed.)*, John Wiley & Sons, New York (, 2001).
41. T. Shinagawa, A. T. Garcia-Esparza and K. Takanabe, *Sci. Rep.*, **5**, 13801 (2015).
42. D.-H. Ha, L. M. Moreau, C. R. Bealing, H. Zhang, R. G. Hennig and R. D. Robinson, *J. Mater. Chem.*, **21**, 11498 (2011).
43. S. Xie, F. Yang, H. Zhang, S. Wang, F. Cheng and X. Lu, *J. Electrochem. Soc.*, **167**, 124512 (2020).
44. W. Huang, H. Sun, H. Shangguan, X. Cao, X. Xiao, F. Shen, K. Mølhave, L. Ci, P. Si and J. Zhang, *Nanoscale*, **10**, 7851 (2018).
45. S. Li, M. Hua, Y. Yang, W. Huang, X. Lin, L. Ci, J. Lou and P. Si, *J. Mater. Chem. A*, **7**, 17386 (2019).
46. X. Zhang, D. Zhang, Y. Chen, X. Sun and Y. Ma, *Chin. Sci. Bull.*, **57**, 3045 (2012).
47. D. Voiry, M. Chhowalla, Y. Gogotsi, N. A. Kotov, Y. Li, R. M. Penner, R. E. Schaak and P. S. Weiss, *ACS Nano*, **12**, 9635 (2018).
48. G. Zhang, G. Wang, Y. Liu, H. Liu, J. Qu and J. Li, *J. Am. Chem. Soc.*, **138**, 14686 (2016).
49. F. Diao, W. Huang, G. Ctistis, H. Wackerbarth, Y. Yang, P. Si, J. Zhang, X. Xiao and C. Engelbrekt, *ACS Appl. Mater. Interfaces*, **13**, 23702 (2021).